Chapter 4. Synthesis of Titanium Dioxide/Cadmium Sulfide Nanosphere Particles for Photocatalyst Applications

Thi Thuy Duong Vu [a,b], *Frej Mighri* [a,b,*], *Abdellah Ajji*[b,c], *Trong-On Do*[a,d]

[a]Department of Chemical Engineering, Laval University, Quebec, QC, G1V 0A6 Canada;

[b]Center for Applied Research on Polymers and Composites (CREPEC);

[c]Department of Chemical Engineering, École Polytechnique of Montreal, C.P. 6079, Montreal, QC, H3C 3A7 Canada;

[d]Centre in Green Chemistry and Catalysis (CGCC).

Published in *Industrial & Engineering Chemistry Research*, **2014**, 53(10), 3888–3897.

Abstract

Semiconductor nanocomposites, which are composed of titanium dioxide (TiO_2) nanorods, cadmium sulphide (CdS) nanoparticles (NPs), and Ni clusters, were synthesized. The following steps were adopted: (i) surfactant-capped TiO_2 nanorods with controlled length were synthesized in autoclave using oleic acid and amino hexanoic acid as surfactants. By using a ligand-exchange procedure, in which nitrosonium tetrafluoroborate ($NOBF_4$) was used to replace the original surfactants, hydrophilic $NOBF_4$-TiO_2 nanorods were obtained; (ii) the resulting nanorods were deposited with CdS NPs and (iii) then deposited selectively with Ni clusters (as cocatalyst) on the nanocomposite surface. Under visible-light illumination of the nanocomposite, the generated electrons from the conduction band of CdS are transferred to TiO_2 via TiO_2/CdS interface, then to metallic Ni cluster. As a result, the electron/hole separation was highly enhanced leading to a Ni-TiO_2/CdS nanocomposite with high photocatalytic performance for the production of hydrogen (H_2).

Résumé

Des nanocomposites semiconducteurs, qui sont composés de nanotubes de dioxyde de titane (TiO_2), de nanoparticules (NPs) de sulfure de cadmium (CdS) et de clusters de Ni, ont été synthétisés. Les étapes suivantes ont été adoptées: (i) des nanotubes de TiO_2 recouverts de surfactant avec une longueur contrôlée, on été synthétisés dans une autoclave en utilisant l'acide oléique et l'acide aminohexanoïque comme les surfactants. En utilisant une procédure d'échange de ligands, dans laquelle le nitrosonium tetrafluoroborate ($NOBF_4$) a été utilisé pour remplacer les surfactants originaux, des nanotubes hydrophiles de $NOBF_4$-TiO_2 ont été obtenus; (ii) les nanotubes obtenus ont été déposés avec des NPs de CdS et (iii) déposés sélectivement ensuite avec les clusters de Ni (comme cocatalyseur) sur la surface du nanocomposite. Avec un éclairage à la lumière visible du nanocomposite, les électrons générés à partir de la bande de conduction du CdS sont transférés au TiO_2 via l'interface TiO_2/CdS, ensuite au cluster métallique du Ni. En conséquence, la séparation électron/trou a été fortement améliorée conduisant à un nanocomposite Ni-TiO_2/CdS de haute performance catalytique pour la production de l'hydrogène (H_2).

4.1. Introduction

As one of the most abundant element with high energy efficiency, hydrogen generated via solar water splitting has currently attracted a particular attention. Hydrogen energy yield is reported up to 122 kJ/g, which is largely higher than that of other fuels, such as gasoline (40 kJ/g)[1]. So H_2 is presently considered as one on the future ideal fuel candidates for the energy generation. Moreover, solar water splitting is environmentally friendly and has a great potential for low-cost and clean hydrogen production. In addition, H_2 can be easily distributed over large distances through pipelines or via tankers. It can also be stored in gaseous, liquid or metal hydride forms, and thus providing a huge market potential.

In a photocatalytic H_2 production reaction from water, the chemical reaction is induced by photo-irradiation in the presence of a photocatalyst. With a relative narrow band gap of 2.4 eV, CdS is one of the sulfide-based semiconductors, which have promising applications in photocatalysis[2–6]. However, CdS alone shows very low H_2 generation rates due to the rapid recombination of photogenerated electrons and holes, which causes a lack of H_2 evolution sites. Good performances were mostly achieved in the presence of noble metal co-catalysts, such as platinum (Pt), palladium (Pd) and nickel (Ni). Among various strategies to improve the photocatalytic activity of CdS, the most efficient method is to promote the charge separation of photogenerated electrons and holes by coupling CdS with other semiconductors with adequate flat potentials, such as TiO_2[7,8], zinc oxide (ZnO)[9] or graphene[10,11]. In such systems, electrons from the conduction band of CdS can be transferred to other semiconductors or graphene, leading to improved electron-hole separation, hence could enhance the generation rate of H_2. TiO_2 has been widely used as a photocatalyst due to its high photostability and oxidation efficiency, and its abundance and non-corrosives. It is also environmental friendly cost effective[12]. With proper band structures, TiO_2/CdS nanocomposite exhibits good properties in photocatalysis, leading to an improved photo-production of H_2 under visible light[13–17].

Herein, we describe new non-noble metal-nanocomposites (NCs) as highly efficient and stable visible-light driven photocatalysts. These NCs are composed of TiO_2 nanorods, CdS NPs, and Ni clusters. An important advantage of TiO_2 nanorod-based nanocomposites

is that CdS NPs are evenly-dispersed on nanorod surface with strong bonding, and cocatalyst Ni clusters are selectively deposited on the surface of these nanorods. This configuration can improve the efficiency of electron transfer from the sensitized CdS NPs to TiO_2 and then to Ni clusters. As anticipated, Ni-TiO_2/CdS nanocomposites developed in the present work exhibit enhanced H_2 production from water under visible light using ethanol as a sacrificial reagent.

4.2. Experimental

4.2.1. Materials

All chemicals were used as received without further purification or distillation. Titanium (IV) butoxide (TB, 97%), oleic acid (OA, 90%), 6-aminohexanoic acid (6AHA), cadmium acetate dehydrate, thioamide and nitrosonium tetrafluoroborate solution ($NOBF_4$) were purchased from Aldrich. Absolute ethanol, N,N-dimethylformamide (DMF), dichloromethane, hexane and toluene, were respectively purchased from Brampton Canada, Fisher Scientific Canada, and Anachemia Canada. All of them were of analytical grade.

4.2.2. Synthesis of length-controlled TiO_2 nanorods using oleic acid and 6-aminohexanoic acid as surfactants

Capped-TiO_2 nanorods were synthesized at low temperature using solvothermal method. Oleic acid (OA), and 6-aminohexanoic acid (6AHA) were used as surfactants with various molar ratio. Mixture of 1mmol TB, 6AHA, OA and absolute ethanol (EtOH) with desired precursor molar ratios were mixed well and stirred for 30 mins under room temperature before being transferred into a Teflon-lined stainless steel autoclave. The autoclave also contained about 5-10 ml EtOH in order to keep equilibrium in the mixture and to avoid any change in EtOH concentration during the crystallization process. The synthesis process was set at 140^{o}C for 18 h. After that, the autoclave was cooled down

slowly to room temperature, and samples were collected and washed several times using ethanol and toluene.

4.2.3. Development of TiO_2 nanorods by Ligand Exchange Reaction

Typically, 5 mL of dichloromethane solution of $NOBF_4$ (0.01M) was added to hexane solvent containing capped-TiO_2 nanorods at room temperature. The mixture was then gently shaken until the precipitation of the TiO_2 nanorods. These nanorods quickly become insoluble and are collected through centrifugation. Then, they were re-dispersed in DMF hydrophilic solvent. To purify the TiO_2 nanorods, DMF solutions were washed through the addition of a mixture of toluene and ethanol 95% until precipitation occurs then followed by centrifugation. This process was repeated few times. Finally, the collected TiO_2 nanorods were dried overnight in oven at 65^{o}C to remove residual solvent molecules.

4.2.4. Synthesis of Colloidal Hybrid TiO_2/CdS nanocomposite

A mixture of 4.5 mmol of $NOBF_4$-capped-TiO_2 nanorods dispersed in 10 ml of DMF, and 9 mmol of Cadmium acetate dihydrate was stirred under room temperature for 2 h. Subsequently, 9 mmol of thioamide were added to the mixture and let under stirring for three more hours in order to ensure a complete reaction. The precipitated TiO_2/CdS nanocrystals were washed few times using toluene and ethanol 95%, and then collected by centrifugation.

4.2.5. Synthesis of Ni-TiO_2/CdS by a Photodeposition method

Typically, $Ni(NO_3)_2$ was added to the solution containing TiO_2/CdS. Because the surface of TiO_2 is negative, positive charge Ni^{2+} is selectively absorbed on the TiO_2 surface, leading to the formation of TiO_2/CdS-Ni^{2+}. This solution is then illuminated with visible light for 1.5h. As the potential of Ni^{2+}/Ni is lower than the conduction band level of

TiO_2, the electrons from the latter can effectively reduce Ni^{2+} species adsorbed on their surface, then forming metallic Ni cluster[18].

4.2.6. Characterization

Transmission electron microscopy (TEM) images of TiO_2 nanorods, and hybrid TiO_2/CdS NCs were obtained on a JOEL JEM 1230 operated at 120 kV. Samples were prepared as follows: a drop of a dilute toluene dispersion of nanocrystals were deposited onto a 200 mesh carbon-coated copper grid then evaporated immediately at ambient temperature. Elemental dispersive spectrum (SEM-EDX) analysis was obtained from a JEOL 6360 instrument working at 3 kV. Powder X-ray diffraction (XRD) patterns of the samples were obtained on a Bruker SMART APEXII X-ray diffractometer equipped with a Cu Kα radiation source (λ = 1.5418 Å) in the 2θ range of 5–20° at a scan rate of 1.0°/min. All samples were dried at 65°C overnight to eliminate guest solvent molecules on the surface of particles before the XRD scan. Fourier transform infrared absorption spectra (FTIR) were measured with a FTS 45 infrared spectrophotometer in the spectral range of 4000–400 cm^{-1}. The thermal analyses of the as-made TiO_2 nanorods, CdS NPs and hybrid TiO_2/CdS NCs were carried out at a heating rate of 10°C/min up to 900°C under an oxygen flow using a Perkin-Elmer TGA thermogravimetric analyzer. The UV−visible spectra of the nanostructures were recorded for the powder sample on a Cary 300 Bio UV−visible spectrophotometer, and pure magnesium oxide (MgO) was used as a blank. ζ-Potential measurements were performed with a Zetasizer Nano ZS in water at 25°C. Nitrogen adsorption/desorption isotherms of the samples were obtained using with a Quantachrome Autosorb-1 system, after degassing at 100 °C and 10-5 mmHg for at least 5 h. The specific surface areas (SBET) of the samples were calculated from adsorption isotherm data using the standard Brunauer−Emmett−Teller (BET) method. XPS characterization was carried out in order to analyze the chemical composition of composite, as well as the electronic state of Ni in the sample. XPS measurement was done in an evacuated ion-pumped chamber at 1×10^{-9} Torr of Kratos Axis-Ultra instrument (UK). The X-ray source is a monochromatic Al source (Al Kα, hv = 1486.6 eV) operated at 300 watts. The binding energy of samples was measured by fixing an internal reference C1s peak at 285.0 eV. For

the separate constituents after background subtraction, all the peaks were deconvoluted by means of standard CasaXPS software.

4.2.7. Photocatalysis characterization (Photocatalytic H_2 evolution)

Before photocatalytic characterization, the surfactants adsorbed on samples were eliminated. These samples were dried overnight at 65^{o}C and used as such for photocatalytic measurement. Visible light-induced H_2 evolution was carried out in 80mL septum-sealed glass vials. A mixture of 20 mg of sample and 3% Ni^{2+} were dispersed well in 27 mL of aqueous solution containing ethanol (25 % wt.). The vial was deoxygenated using nitrogen, and then placed in front of 300 W Xe-lamp with a 420 nm cut-off filter (FSQ-GG420) for catalytic reaction. Gaseous products were then identified by collecting 0.5 ml of the gas in the headspace of the vials. This gas was then analyzed by gas chromatography (GC) using a thermal conductivity detector (TCD) for the quantification of H_2 with N_2 as the carrier.

4.3. Results and Discussions

Scheme 4.1 shows the procedure adopted for the synthesis of surfactant capped-TiO_2 nanorods by the hydrolysis of a titania precursor followed by a solvothermal reaction in autoclave. First, an ethanol solution of titanium (IV) butoxide (TB) was modified by hydrolysis with OA and 6AHA as surfactants. The hydrolysis process helped to yield three-dimensional polymeric titania skeletons, which acted as the seeds for titania growth. In order to obtain the desired TiO_2 uniform sizes of particles, the subsequent solvothermal process was carefully controlled with pre-setting the reaction time (18 hrs) and temperature (140^{o}C). It was observed that TiO_2 nanorods were always achieved with the use of OA and 6AHA as surfactants.

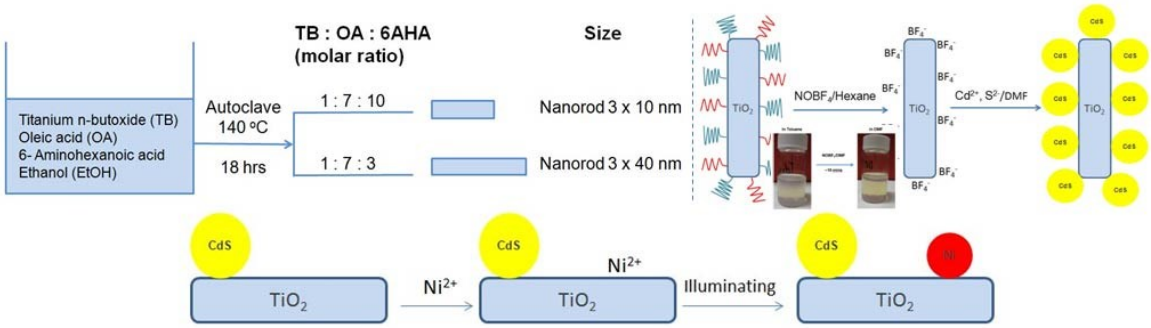

Scheme 4.1. Sketch for the preparation of TiO_2/CdS nanocomposites.

4.3.1. TEM, FTIR and BET characterization

Figure 4.1 shows TEM image of the obtained TiO_2 nanorods before sonication. As seen in the TEM image, these nanorods were attached together in a parallel configuration to form big aggregation. This is different from the results obtained by Dinh et al.[19] who showed well dispersed TiO_2 nanorods by using OA and oleylamine as surfactants. The aggregation obtained in our approach may be due to the replacement of oleylamine by 6AHA surfactant.

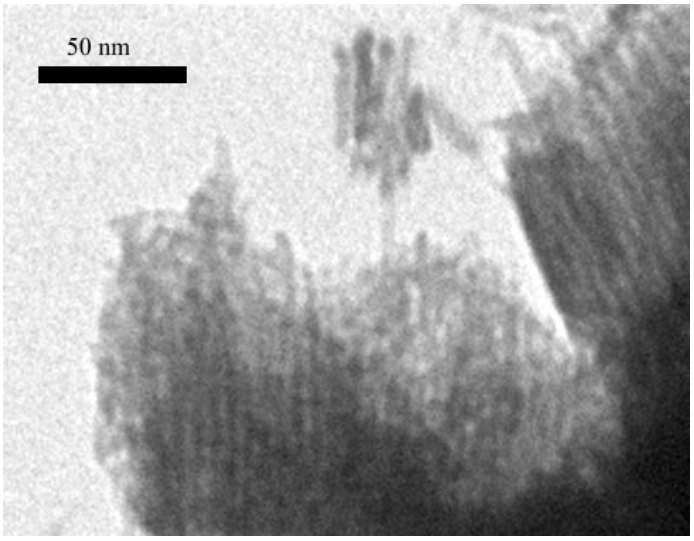

Figure 4.1. TEM image of the synthesized TiO_2 nanorods before sonication.

Figure 4.2 also shows TEM images of TiO_2 nanorod samples obtained with different molar TB:OA:6AHA ratios after few minutes of sonication. As seen in Figure 2,

by varying the molar ratio between TB, OA and 6AHA, different sizes of TiO_2 nanorods were observed. For a molar TB:OA: 6AHA ratio of 1:7:3, TiO_2 nanorods of 3x40 nm were achieved (Figure 2a). When the concentration of 6AHA was increased from 3 to 10 (e.g., from1:7:3 to 1:7:10), while the TB and OA concentrations kept the same, the shape of TiO_2 nanorods did not change, however the length of the nanorod was decreased from 40 to 10 nm (Figure 2b). Hence, it could be assumed that the length of TiO_2 nanorods is controlled by the molar ratio OA:6AHA. Also, it should be mentioned that OA and 6AHA surfactants have selective bindings to the different faces of TiO_2. Joo et al.[20] reported that OA binds strongly to the TiO_2 {001} faces, while 6AHA binding is more favored on {101} faces. When the concentration of 6AHA is high (molar ratio OA:6AHA = 7:10), the strong adhesion of 6AHA to the low surface energy {101} face, compared to the adhesion of OA to {001} face, leads to a less progressive TiO_2 growth along {001} direction to form TiO_2 nanorods with short length. By decreasing the molar concentration of 6AHA, the adhesion of 6AHA to the low surface energy {101} decreases while the adhesion of OA to {001} is kept the same. The growth along {001} is then preserved, leading to longer TiO_2 nanorod shape[21].

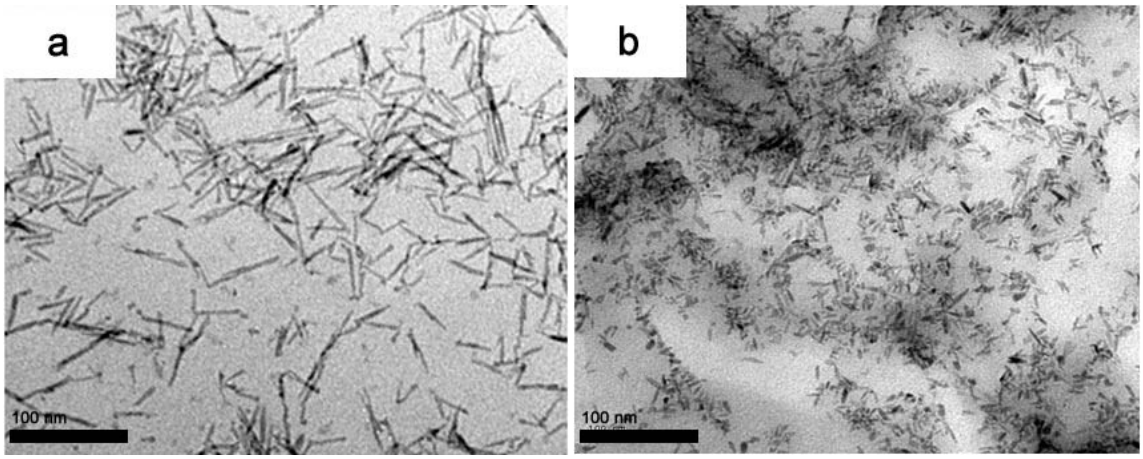

Figure 4.2. TEM images of synthesized TiO_2 nanorods after sonication a) 3x40 nm nanorods for TB:OA:6AHA molar concentration of 1:7:3, and b) 3x10nm nanorods for TB:OA:6AHA molar concentration of 1:7:10.

Since OA and 6AHA were used as capping agents, the hydrophobic surfactant capped- TiO_2 nanorods were soluble in nonpolar hydrophobic solvents, such as toluene and hexane. However, after being treated with dichloromethane solution of $NOBF_4$, TiO_2 nanorods precipitated immediately in hexane solvent after gentle shaking indicating that $NOBF_4$ has replaced the original hydrophobic surfactant capped to the nanorod surface. This also indicates a dramatic change in surface properties of these NPs, from hydrophobic to hydrophilic. As seen in Figure 4.3, it was observed that $NOBF_4$ capped-TiO_2 nanorods were easily re-dissolved in DMF solvent as well as in water. This is considered as an advantage during the deposit process of CdS on the surface of TiO_2 nanorods since both cadmium acetate and thioamide are well dissolved in DMF. A higher dispersion of the initial precursors in the media (TiO_2, Cd^{2+}, S^{2-}) increases the chance to achieve uniform TiO_2 nanorods with a higher dispersion of CdS on their surface.

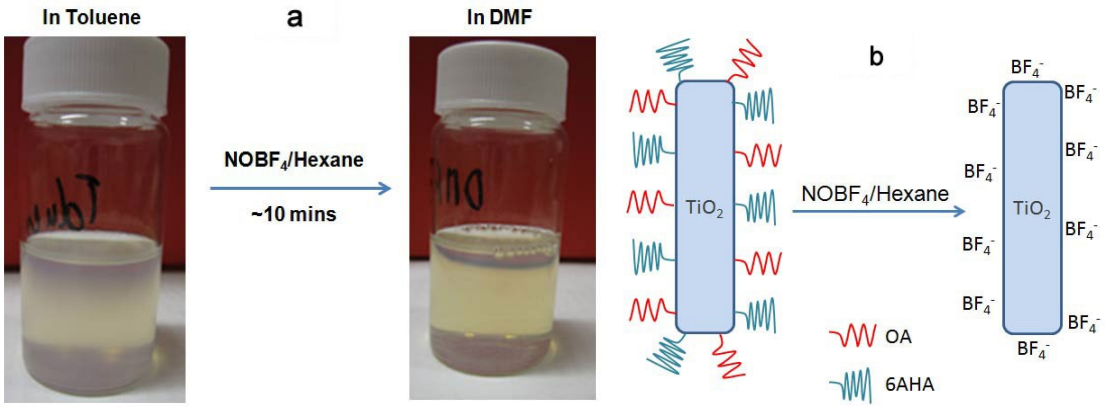

Figure 4.3. (a) Surfactant-capped TiO_2 nanorods dissolved in toluene; (b) TiO_2 nanorods after $NOBF_4$ treatment dissolved in DMF.

In order to analyze the surface properties of TiO_2 nanorods, FTIR characterization was done for the samples before and after surfactant treatment. The corresponding results are shown in Figure 4.4. FTIR spectra of the capped TiO_2 nanorods before surface treatment with $NOBF_4$ and those of OA and 6AHA surfactants are shown in Figure 4.4a. The small peaks at 3004 cm^{-1} were observed in the both FTIR spectra of OA and 6AHA corresponding to the stretching of =C-H bond. The sharp vibrations bands at 2916 and 2857 cm^{-1} are attributed to the asymmetric and symmetric C-H bonds in methylene groups

(CH_2), respectively.[22]The peaks at 1714 and 1282 cm^{-1} in the spectrum of OA are assigned to C=O and C-O stretching and those appearing at 1463 and 936 cm^{-1} are due to in-plane and out-of plane O-H. Compared to the commercial P25-TiO_2, our synthesized TiO_2 nanorods are identified by the additional peaks at 3004, 2922, 2853, and 1465 cm^{-1} due to the presence of capping ligand on the surface. In addition, the peak appearing at 1608 cm^{-1} indicates the existence of carboxylic acid salt on the surface of surfactant capped-TiO_2 nanorods, which is the result of the reaction between the OA surfactant and TiO_2 during the solvothermal process. Furthermore, a weak peak at 1041 cm^{-1} in the sample of surfactant capped-TiO_2 nanorods, which corresponds to that of C-N bonds in the amine groups, proves the existence of amine on their surface (resulting from 6AHA surfactant).

Figure 4.4(b), shows the FTIR spectrum of the TiO_2/CdS NCs after surface treatment. No essential peak characteristic of -C-H stretching vibration at 2800-3000 cm^{-1} was observed after CdS deposition, as compared to that of the sample before deposition. This could be due to $NOBF_4$ treatment process where CdS deposition was able to remove some residues of OA and 6AHA molecules attached to TiO_2 nanorods surface (see Figure 4). As will be presented later (TGA characterization), this could explain the difference of weight loss between TiO_2 nanorods and TiO_2/CdS nanocomposite. Furthermore, in comparison with the FTIR spectrum of TiO_2 nanorods before $NOBF_4$ treatment, there is a small peak at around 1000 cm^{-1}, which is assigned to BF_4^- anions. Furthermore, no peak is observed around 2100-2200 cm^{-1}, which is normally ascribed to NO^+. This is an indication that surfactant exchange was between the organic ligands and inorganic BF_4^-, not with NO^+. The big peak at around 3050 cm^{-1} on the FTIR spectrum of TiO_2/CdS, which is similar to the peak observed for commercial TiO_2 nanorods, is attributed to the water absorbed on the surface of TiO_2/CdS nanocomposite.

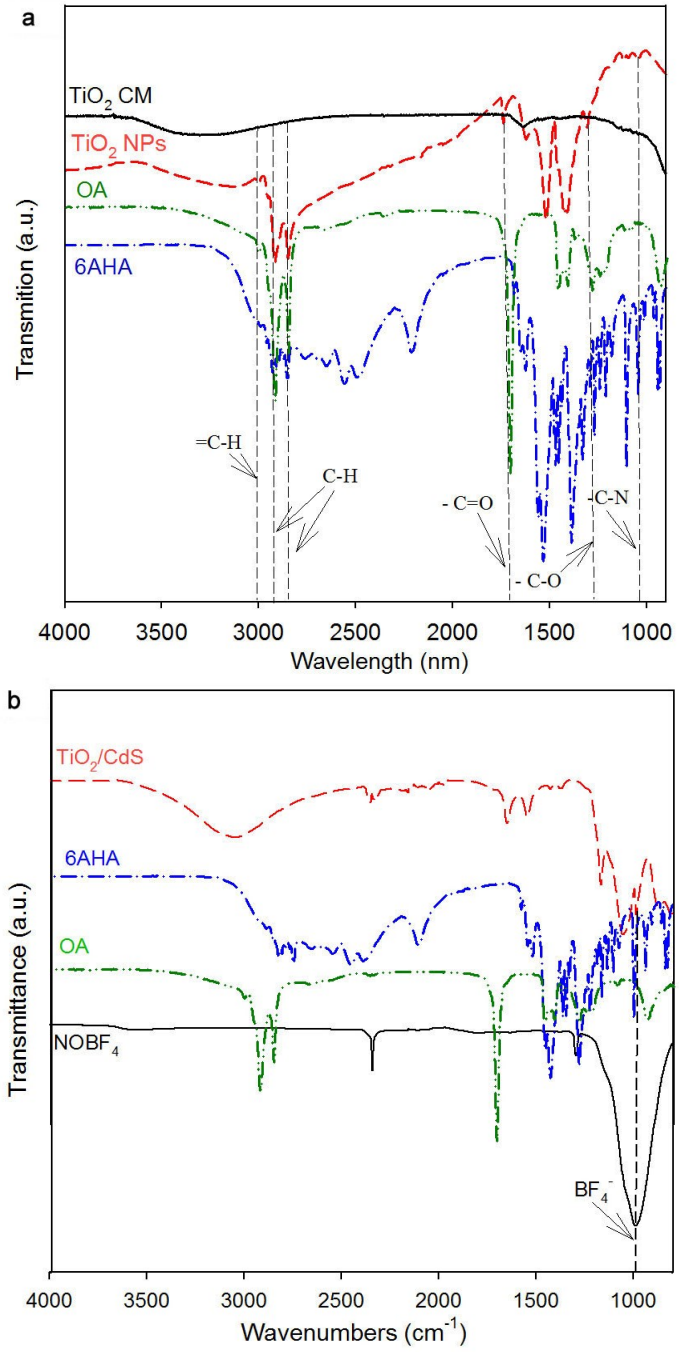

Figure 4.4. FTIR of (a) capped-TiO_2 nanorod synthesized using OA and 6AHA as surfactants; and (b) TiO_2/CdS nanoparticles.

Figure 4.5 shows TEM image and Brunauer–Emmett–Teller (BET) adsorption/desorption isotherm curves for the sample of TiO_2/CdS nanocomposites. As seen in Figure 5(a), TiO_2/CdS nanoparticles were aggregated to form hollow nanospheres

with a uniform diameter of around 150 nm. When water sonication was performed, hollow nanospheres were separated from each other. However, single nanospheres were not separated into single NPs by sonication at low frequency ultrasound. Because the TiO_2/CdS hollow nanospheres are composed of a large number of nanoparticles, a high surface area can be expected, as shown in Figure 4.5b. The BET specific surface area is 146 m^2/g, which is much higher than that of TiO_2 nanorod (27.5 m^2/g) and of CdS cubic (34.7 m^2/g). The surface area results are in agreement with the observation from the isotherm figure, which shows that the isotherms of TiO_2/CdS shift up compared to those of TiO_2 and CdS.

The pore size distribution curves (see inset, Figure 4.5(b)) calculated from the desorption branch of the nitrogen isotherms by the BJH method show a wide range of pore diameters (from 5 to 237 nm) with a peak at a pore diameter of about 166 nm. Meanwhile, a distinct hysteresis loop can be observed between adsorption and desorption branches, in the range of 0.8 to 1 nm, which is an indication of mesostructured the TiO_2/CdS nanospheres[23,24].

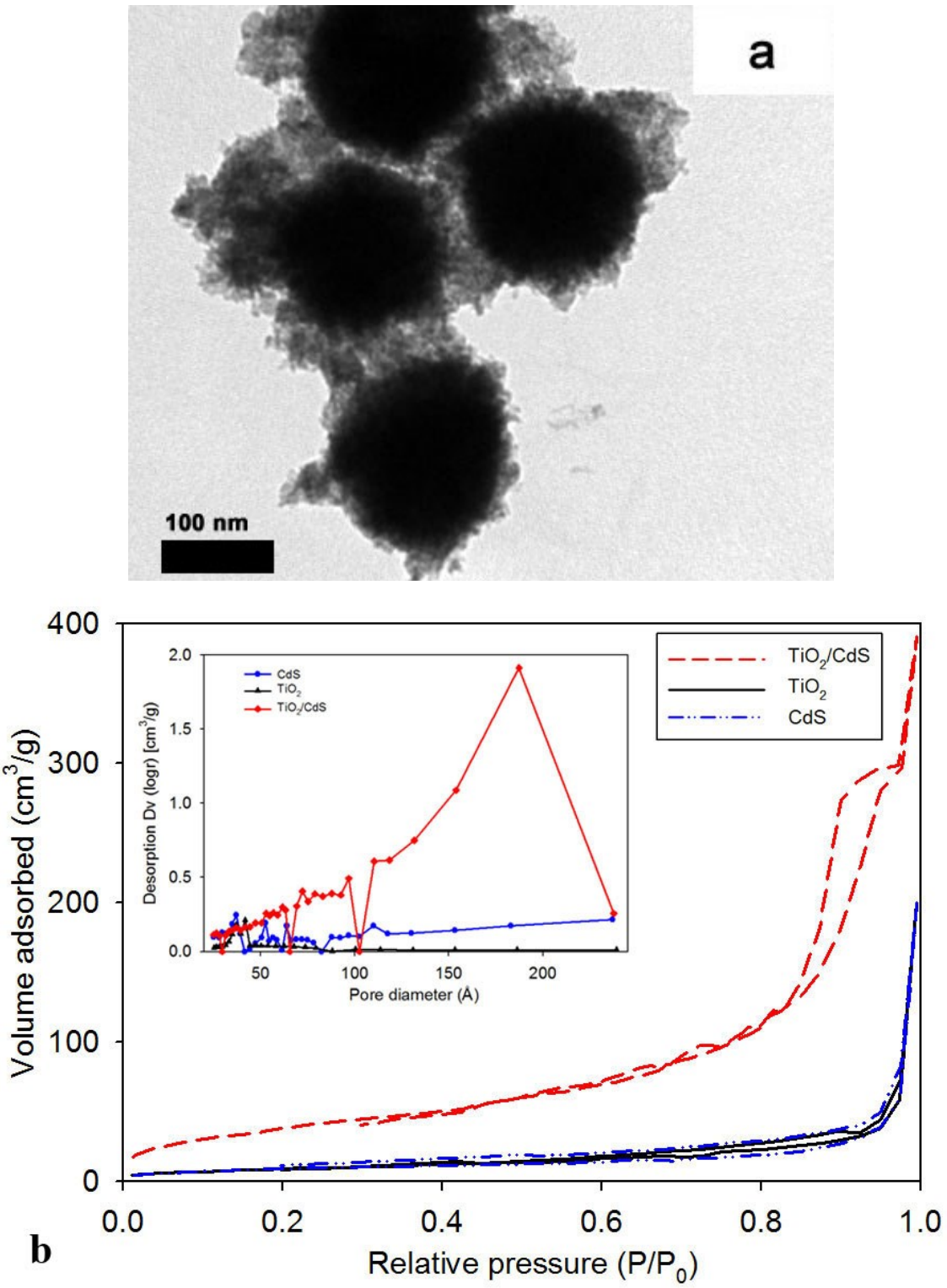

Figure 4.5. (a) TEM image of TiO_2/CdS nanocomposite, and (b) BET characterization of TiO_2, CdS, and TiO_2/CdS nanocomposite with the inset is their corresponding pore size distribution

4.3.2. XRD characterization

Figure 4.6 shows XRD patterns of TiO_2 nanorods, CdS NPs and TiO_2/CdS nanocomposite. XRD patterns of TiO_2 nanorods exhibit strong diffraction peaks at 25° and 48°, indicating TiO_2 anatase phase. All peaks were in good agreement with the standard spectrum for TiO_2 (JCPDS no: 88-1175 and 84-1286). Meanwhile, it is known that CdS NPs possess the hexagonal phase with (002) as the preferential crystalline plane with two main peaks at 28.3º (101 planes) and 48.1º (103 planes)[25], while the cubic phase has three main peaks at 26.5º (111 planes), 43.9º (220 planes) and 51.9º (311 planes)[13]. Hence, with those peaks shown in the XRD pattern of CdS NPs, we can conclude that CdS NPs are in cubic phase.

XRD patterns of the TiO_2/CdS nanocomposites confirm the presence of CdS and TiO_2. However, when mixed with high concentration of CdS NPs, the intensity of the diffraction peaks at 48° was very low, which could be due to the attachment of CdS on the surface of TiO_2 nanorods. In the XRD spectrum of our TiO_2/CdS nanocomposite, three broad and symmetric peaks were observed at 2Θ = 26.5º (111 planes), 43.9º (220 planes), and 51.9º (331 planes) corresponding to the cubic phase of CdS. The absence of planes referring to hexagonal structured CdS indicates the presence of only cubic CdS nanoparticles in the sample. Furthermore, the broadening of the peaks is due to the CdS nanosize in the TiO_2/CdS nanocomposite.

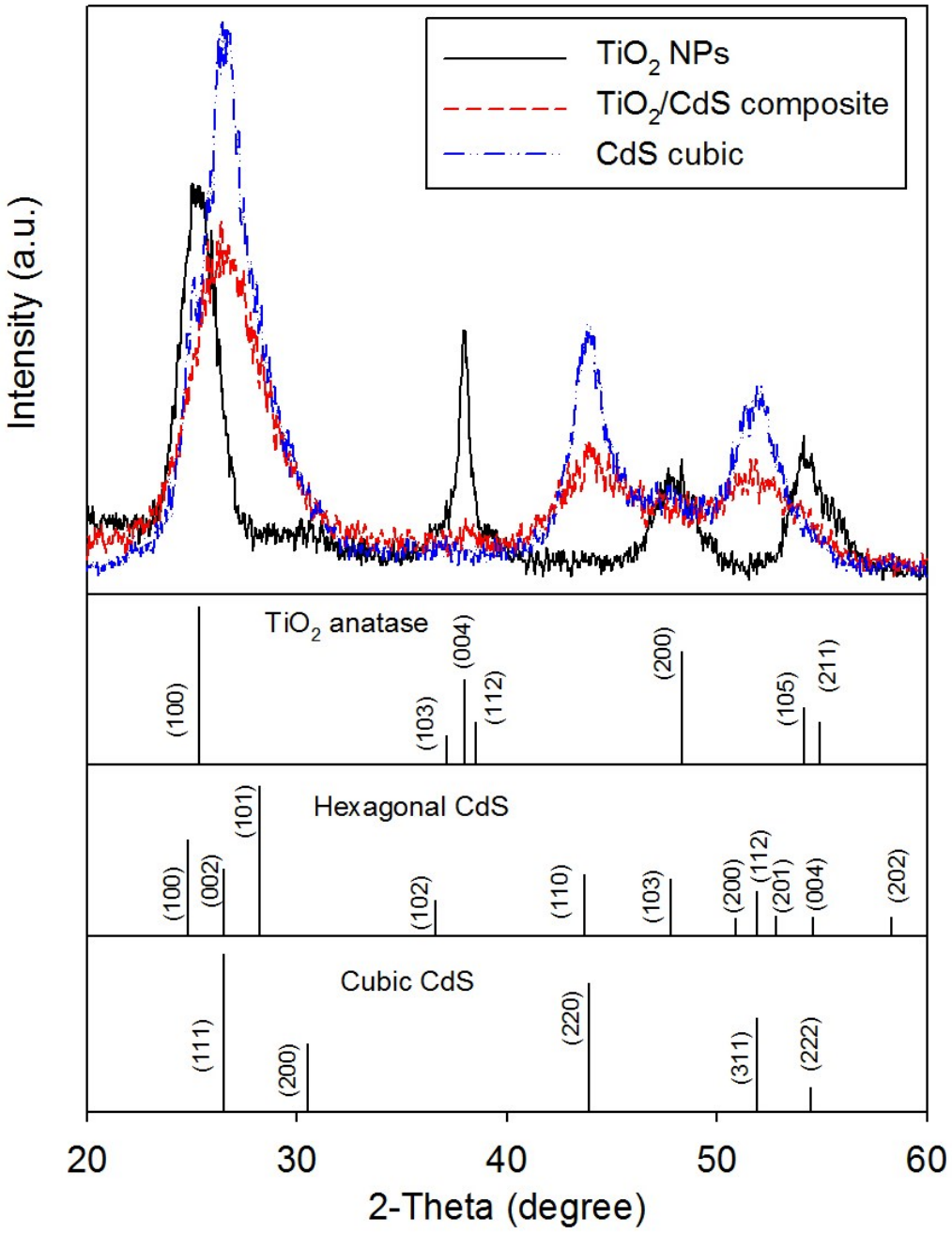

Figure 4.6. XRD characterization of a) TiO_2 nanorod b) TiO_2/CdS nanocomposite.

4.3.3. XPS and SEM-EDX characterization

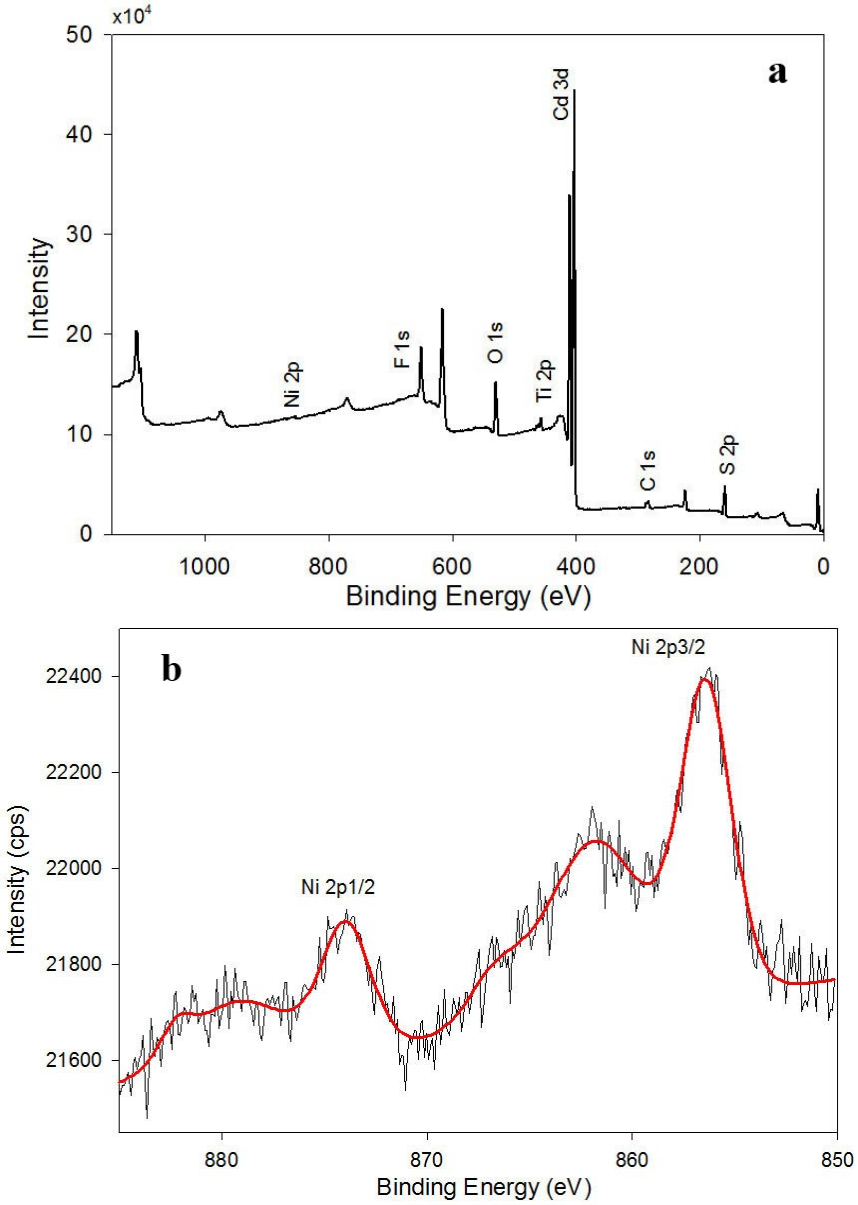

Figure 4.7. (a) XPS characterization of Ni-TiO_2/CdS nanocomposite (b) High-resolution XPS of Ni

The XPS survey spectrum (Figure 4.7(a)) shows the existence of Ti, O, Cd, S, Ni and C elements in the sample. Also, the high-resolution XPS spectrum of Ni 2p3/2 peak at 856.4 eV confirms the presence of Ni in the sample (Figure 4.7b), mainly from NiO.[26,27] The formation of NiO could be due to the photo-induced electrons in the conduction band

of TiO_2 transferred to Ni^{2+} clusters causing the reduction of a part of Ni^{2+} clusters to NiO atoms due to their instability in the air.[27] In addition, the Ti2p and O1s peaks are respectively found at 458.6 and 530.95 eV, which are compatible with the assignment to TiO_2. Cd3d (405.1eV) and S2p (161.95 eV) peaks are reported to be compatible with CdS. The observation of C1s element is due to the surfactant capped on the surface of the sample, and also from the adventitious hydrocarbon in the XPS instrument itself. The XPS peak at 686.91eV is ascribed to F^- ions coming from $NOBF_4$ during surfactant treatment process.

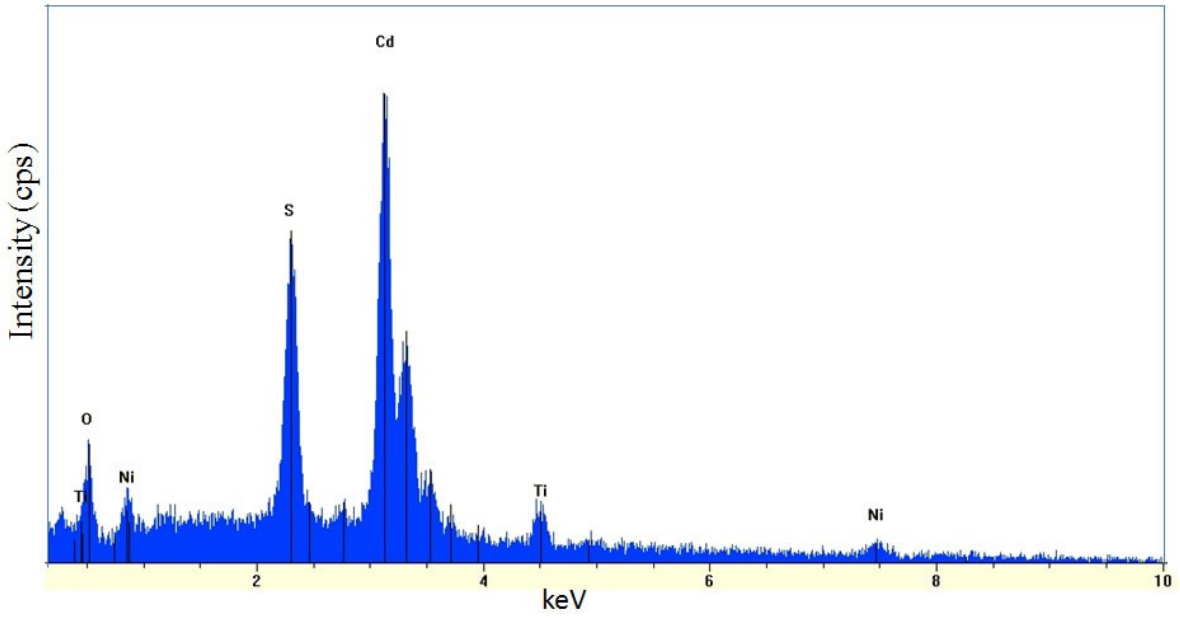

Figure 4.8. SEM-EDX characterization of Ni-TiO_2/CdS nanocomposite

The presence of Ni in the sample was also confirmed from the SEM-EDX elemental analytical spectrum (Figure 4.8). This spectrum shows that the intensity of Ni peak is small compared to the other elements. This is due to the small amount of Ni cluster deposited on the TiO_2/CdS composite, which is only 3% wt.

4.3.4. UV/Vis and Photoluminescence (PL) characterizations

The optical properties of TiO_2 nanorods before surface treatment and TiO_2/CdS nanocomposites were investigated by UV/Vis absorption and photoluminescence (PL)

characterization techniques. The UV-visible absorption spectrum (Figure 4.9(a)) has been performed to measure the photo-response of TiO_2 nanorods after their loading with CdS. The absorption edge for anatase TiO_2 nanorod is approximately 380 nm (3.12 eV), which has no significant absorption in visible-light region. However, the spectrum of CdS exhibits a broad absorption band around 530 nm (2.32 eV), indicating the effective photo-absorption property in the visible region. Basically, the spectrum of TiO_2/CdS nanocomposite is a combination of TiO_2 and CdS spectra. The absorption edges of TiO_2/CdS nanocomposite is approximately 547 nm (2.23 eV), which is around 15 nm red-shift than that of CdS. This probably results from the coupling between CdS and TiO_2.

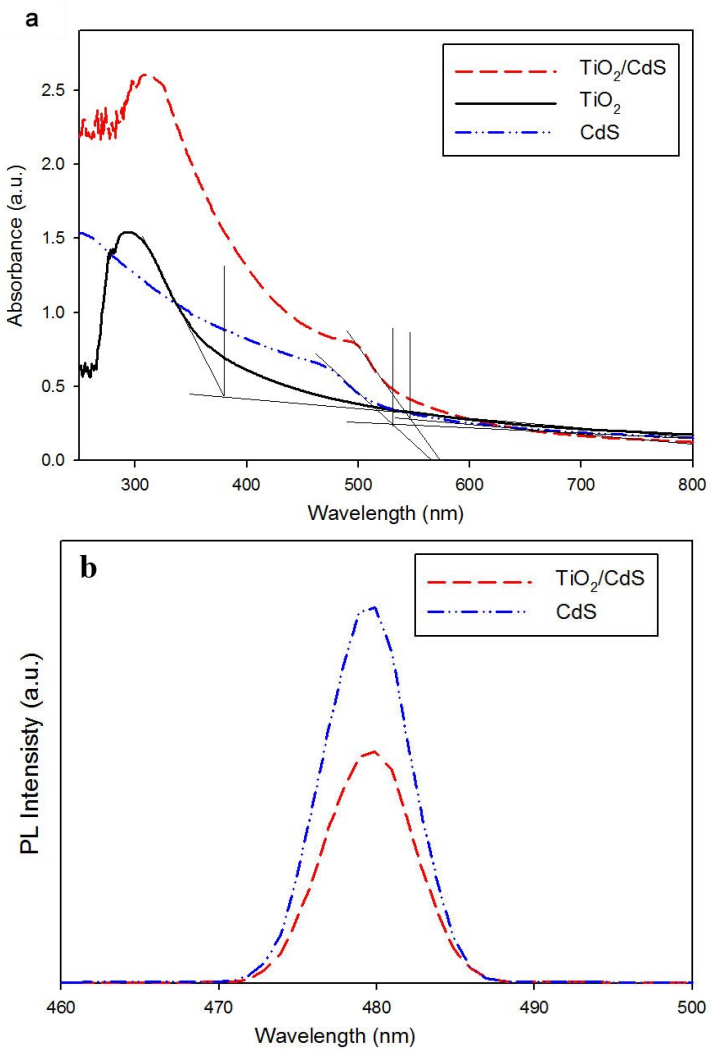

Figure 4.9. (a) UV-Vis spectra of TiO_2, CdS and TiO_2/CdS (b) Photoluminescence (PL) emission spectra under excitation at a wavelength of 380 nm for CdS and TiO_2/CdS nanocomposite.

Figure 4.9(b) shows the PL emission spectra for CdS and TiO_2/CdS nanocomposites at room temperature under light excitation at a wavelength of 380 nm. According to the PL of both CdS and TiO_2/CdS sample, PL peak of TiO_2/CdS exhibited much weaker intensity than of that of CdS. The decrease in PL intensity indicates a better PL quenching, which also indicates a decrease in light emission of the material or a coupling between CdS and TiO_2 with a better charge transfer between these two nanoparticles. As discussion above, the efficient charge transfer from CdS to TiO_2 conduction band could effectively separate the photo-induced electrons from holes in the CdS semiconductor. Thus, the decrease in PL intensity also could be ascribed to the lower recombination probability of photo-induced electrons and holes in TiO_2/CdS nanocomposites.[28]

4.3.5. Thermal Gravimetric (TGA) and ζ-potential characterization

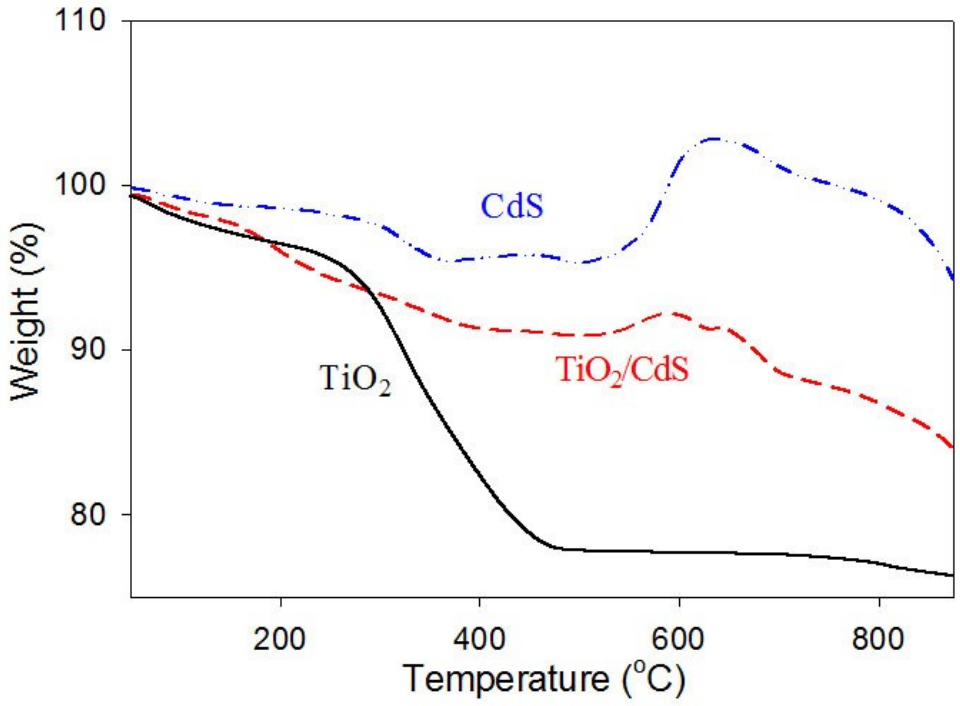

Figure 4.10. TGA characterization of (black) TiO_2 nanorods (blue) CdS NPs (red) TiO_2/CdS nanocomposite.

Thermal gravimetric characterization of synthesized capped TiO_2 nanorods, CdS NPs, and TiO_2/CdS nanocomposites are summarized in TGA curves of Figure 4.10, which were obtained at a heating rate of 10 ºC/min under O_2 atmosphere. All the three curves show an initial weight loss starting at around 50ºC, which could be attributed to the water absorbed on the surface of the nanoparticles. For TiO_2 nanorods, the most significant weight loss obviously occurred between 200 and 480ºC and corresponds to OA surfactants. For higher temperatures (>480ºC), the very small weight loss could be attributed to the decomposition of residual product traces that forms a sheath over the TiO_2 nanorods. For CdS NPs, the TGA spectrum shows that the main mass decrease occurred below 400ºC, which could be mainly due to the evaporation of residual solvent. A non-negligible gain in mass was also observed between 400 and 750°C, which is an indication of the formation of cadmium sulphate ($CdSO_4$) through the following reaction (Equation 1).[29] The decomposition of $CdSO_4$ starts at 750ºC leading to a further decrease in mass.

$$CdS\ (g) + 2O_2 \rightarrow CdSO_4 \qquad \textbf{(4-1)}$$

he TGA behavior of TiO_2/CdS nanocomposite is basically a combination of TiO_2 and CdS behaviors. The weight loss below 200ºC could be attributed to the water absorbed on the surface of particles, while weight loss from 200 to 400ºC could be due to the loss of the rest of surfactant on the surface of TiO_2. The mass increase observed at the same temperature level corresponding to the increase in CdS mass, is due, as mentioned above, to the formation of the intermediate product, $CdSO_4$.

The ζ-potential curves of TiO_2 nanorods before and after $NOBF_4$ treatment, CdS NPs, and TiO_2/CdS nanocomposites are shown in Figure 4.11. According to these curves, the charge surface potential of TiO_2 nanorods before surfactant exchange was zero at pH=5. However, when treated with $NOBF_4$, the surface of TiO_2 nanorods was negatively charged, which is in agreement with the results reported by Dong et al.[30] Since the surface of TiO_2/CdS is negatively charged, Ni clusters were selectively deposited (by using photodeposition technique) as co-catalysts on the surface of TiO_2/CdS composite. In this case, Ni^{2+} is selectively adsorbed on the surface of TiO_2 nanorods, not on the surface of CdS (because the ζ-potential of CdS is zero), due to the electro kinetic potential preferable

in colloidal systems. Under visible light illumination, the generated electrons from the conduction band of CdS are transferred to the conduction band of TiO_2. Because the conduction band level of Ni^{2+}/Ni is lower than that of TiO_2, the electrons from the conduction band of TiO_2 are able to reduce Ni^{2+} to form metallic Ni clusters on the surface of TiO_2 nanorods (Scheme 4.1).

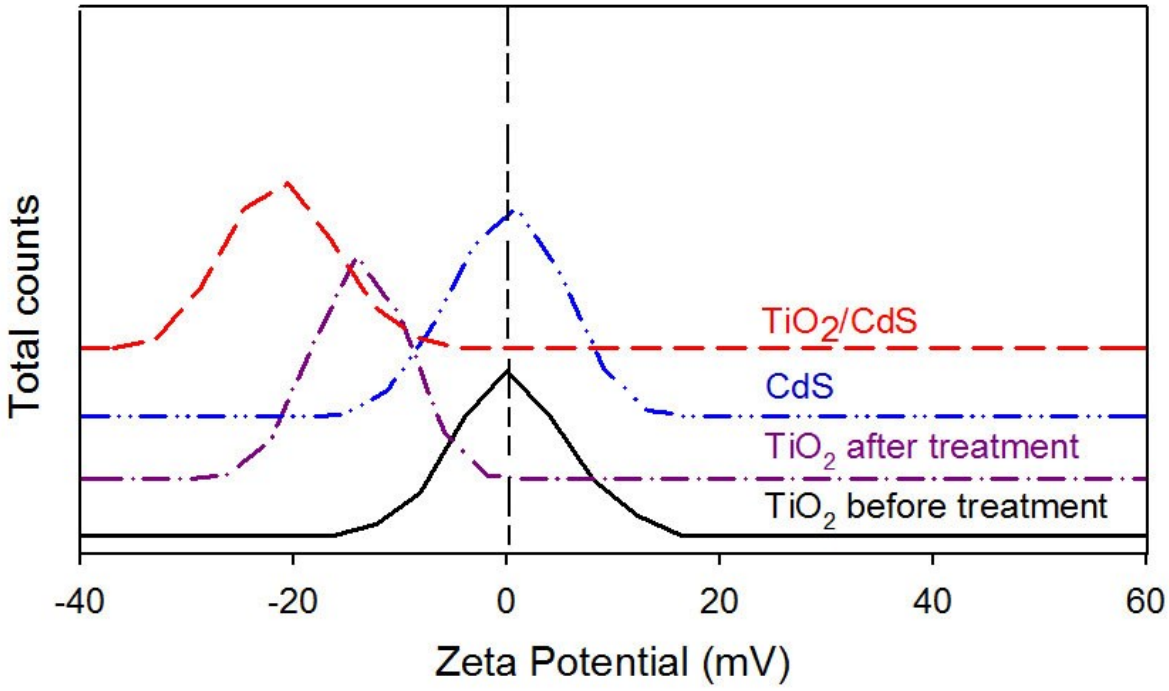

Figure 4.11. ζ-Potential distributions in aqueous solution at pH~5 of TiO_2 nanorods before and after treatment with $NOBF_4$ surfactant; CdS NPs, and TiO_2/CdS nanocomposite.

4.3.6. Photocatalytic activity

The photocatalytic activity of TiO_2, CdS, and TiO_2/CdS nanocomposite with Ni co-catalyst for H_2 generation were carried out under visible light irradiation ($\lambda > 420$ nm) using ethanol as sacrificial reagent. As seen from Figure 12a, TiO_2 nanorods are not able to generate H_2 because TiO_2 nanorods do not absorb visible light and consequently could not generate electron-hole to support the H_2 evolution. Beside, CdS alone shows very low H_2 generation rates, only 0.77 $\mu mol \bullet h^{-1} \bullet g^{-1}$ after 4.5 h of reaction. The low rate could be due to

the rapid recombination of photogenerated electrons and holes, which resulted in the lack of H_2 evolution sites.[31,32] The coupling of CdS with TiO_2 nanorods shows a big improvement in H_2 production; around 33.63 $\mu mol \bullet h^{-1} \bullet g^{-1}$ of H_2 were evolved, which is around 44 times higher than the production for Ni-CdS system. The rate of Ni-TiO_2/CdS photocatalytic activity is also reported to be faster compared to that of Ni-CdS, which could be due to a better charge transfer between CdS and TiO_2, as shown and discussed above (Figure 4.9). The photocatalytic performance of TiO_2/CdS without Ni-cocatalyst using ethanol as sacrificial reagent was also carried out, however, the H_2 production evolution maybe was too low, and so we would not be able to detect the signal of activity. In another word, without using Ni as cocatalyst, the composite TiO_2/CdS is not active for photocatalytic H_2 production using visible light.

To investigate the stability of Ni-TiO_2/CdS samples, a series of tests composed of 4 cycles with intermittent deoxygenation were carried out without catalyst regeneration. Between each cycle, the reaction system was bubbled with N_2 in order to remove H_2. As shown in Figure 4.12(b), the results show good stability for the photocatalyst up to 15 h of irradiation without noticeable catalytic de-activation; however, after 15 hours of reaction, the activity is decreased by about 50%. Even though the photocatalyst was decreased after 15 h of irradiation, this achievement is still considered as a good improvement for the photocatalytic activity of metal sulfides, which are often unstable for conventional CdS photocatalysts, due to the reduction of metal cations in metal sulfides by generated electrons, and the oxidation of S^{2-} by generated holes.[31–33]

In Ni-TiO_2/CdS nanocomposite, with the support of TiO_2 nanorods, the photo-oxidation is avoided due to the electrons transfer from the conduction band of CdS to that of TiO_2 and then to the metallic cocatalyst (Ni), therefore it would prevent Cd^{2+} from reduction. In addition, under visible light illumination, only CdS with small bandgap energy of 2.4 eV can generate holes in the valence band (VB). However, because the VB of CdS (+1.5 V vs. SHE) is smaller than the VB of TiO_2 (+ 3.2 V vs. SHE),[34,35] these holes in the VB of CdS cannot be transferred to the VB of TiO_2. Thus, Ni clusters, which are only located on the surface of TiO_2, cannot be oxidized by holes in the VB of CdS NPs. Therefore, with those mentioned special features above, it is not surprising to see that Ni-

TiO_2/CdS nanocomposite exhibits not only high activity, but also good stability in the photocatalyst production of H_2 up to 15 h of irradiation.

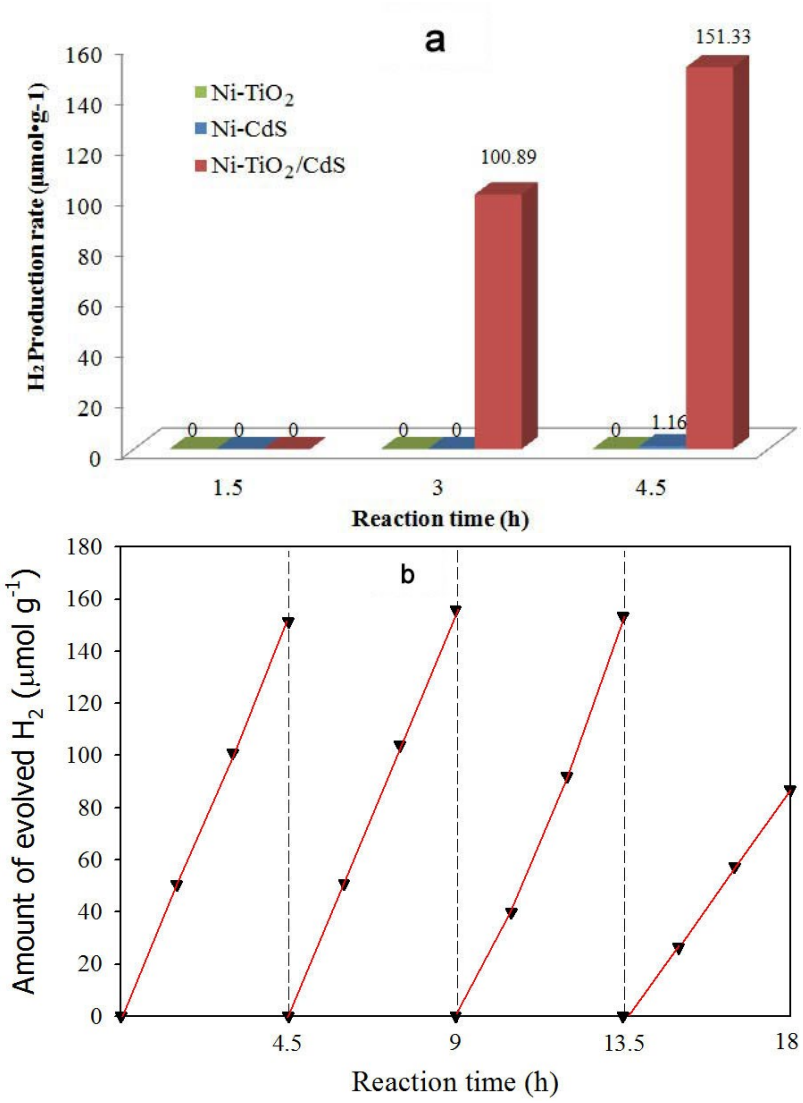

Figure 4.12. (a) Comparison of the activity of H_2 evolution using different photocatalysts; (b) H_2 production from TiO_2/CdS-Ni photocatalyst monitored over 18 h. Each 4.5 h, the reaction system is bubbled with N_2 to remove the H_2 inside.

The mechanism of H_2 production activity of Ni-TiO_2/CdS under visible light is illustrated in Figure 4.13. The full mechanism could be similar to the mechanism of Pt-TiO_2/CdS, which was reported in literature.[36] When the coupled TiO_2 and CdS semiconductors are activated under the visible light, electrons and holes are generated in

the conduction and valance bands of CdS. Furthermore, due to the different bandgap positions, the generated electrons from the conduction band of CdS are transferred towards TiO_2 conduction band. As the Ni clusters are preferentially attached on TiO_2 nanorod instead of CdS NPs, they would be able to cap the electron from the conduction band of TiO_2, and act as H_2 evolution.

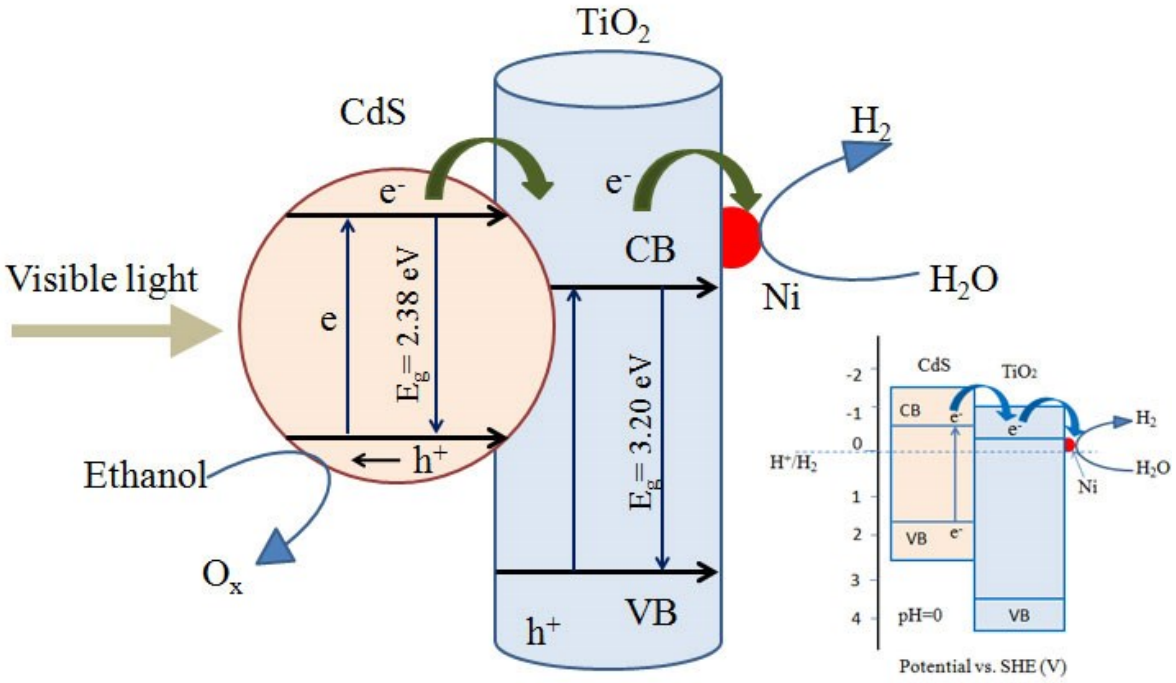

Figure 4.13. Mechanism illustration of the activity of Ni-TiO_2/CdS under visible light for the production of H_2, inset is the potential redox energy corresponding to CdS, TiO_2 and H^+/H_2

Meanwhile, the holes at the valance band of CdS are responsible for oxidizing ethanol and may also anodically auto-corrode the CdS particles[37,38]. If the photogenerated holes do not react quickly with Cd–OH groups or ethanol, the photo-corrosion of CdS occurs and induces a release of cadmium ion in solution leading to the formation of cadmium hydroxide layer on the surface of the CdS particles, as shown by the following equation:

$$CdS + H_2O \rightarrow H_2 + Cd^{2+} + S + 2OH^- \quad \textbf{(4-2)}$$

Also, if the surface of CdS NPs is covered with cadmium hydroxide, this causes sulfide vacancies saturation; hence the holes can no longer be trapped. The recombination

of generated electrons and holes will then be faster[39]. With those two reasons, it would be expected to see a decrease in the photocatalysis activity of the Ni-TiO_2/CdS system after 15h of reaction.

4.4. Conclusions

In conclusion, we developed a new hybrid photocatalytic system for the production of H_2 under visible light illumination using ethanol as a sacrificial agent, which was based on TiO_2 nanorods, CdS nanoparticles and Ni cluster cocatalyst. In a first time and due to the fact that OA and 6AHA surfactants have selective bindings to the different faces of TiO_2 , different sizes of TiO_2 nanorods were obtained varying the molar ratio between TB, OA and 6AHA. A three step synthesis process was then used to develop the TiO_2/CdS-Ni nanocomposite photocatalyst. Under visible-light illumination and due to the fact that electron-hole separation was highly enhanced, the developed TiO_2/CdS-Ni photocatalyst showed a high photocatalytic performance for the H_2 production, which was around 44 times higher than that of Ni-CdS. In addition, this hybrid composite photocatalyst appeared to exhibit a high photocatalytic performance for the production of hydrogen (H_2).

Acknowledgements

The authors would like to thank the Natural Sciences and Engineering Research Council of Canada (NSERC) for financial support of this work.

4.5. References

(1) Liao, C.-H.; Huang, C.-W.; Wu, J. C. S. *Catalysts* **2012**, *2*, 490–516.

(2) Wang, D.; Li, D.; Guo, L.; Fu, F.; Zhang, Z.; Wei, Q. *J. Phys. Chem. C* **2009**, *113*, 5984–5990.

(3) Rao, B. S.; Kumar, B. R.; Reddy, V. R.; Rao, T. S. *Chalcogenide Lett.* **2011**, *8*, 177–185.

(4) Matsumura, M.; Furukawa, S.; Saho, Y.; Tsubomura, H. *J. Phys. Chem.* **1985**, *89*, 1327–1329.

(5) Chen, X.; Shangguan, W. *Front. Energy* **2013**, *7*, 111–118.

(6) Rajendran, V.; Lehnig, M.; Niemeyer, C. M. *J. Mater. Chem.* **2009**, *19*, 6348.

(7) Daghrir, R.; Drogui, P.; Robert, D. *Ind. Eng. Chem. Res.* **2013**, 130226090752004.

(8) Xiang, Q.; Yu, J.; Jaroniec, M. *J. Am. Chem. Soc.* **2012**, *134*, 6575–6578.

(9) Wang, X.; Liu, G.; Chen, Z.-G.; Li, F.; Wang, L.; Lu, G. Q.; Cheng, H.-M. *Chem. Commun. (Camb).* **2009**, 3452–3454.

(10) Li, X.-H.; Zhang, J.; Chen, X.; Fischer, A.; Thomas, A.; Antonietti, M.; Wang, X. *Chem. Mater.* **2011**, *23*, 4344–4348.

(11) Xiang, Q.; Yu, J. *J. Phys. Chem. Lett.* **2013**, *4*, 753–759.

(12) Chen, X.; Mao, S. S. *Chem. Rev.* **2007**, *107*, 2891–2959.

(13) Li, G.-S.; Zhang, D.-Q.; Yu, J. C. *Environ. Sci. Technol.* **2009**, *43*, 7079–7085.

(14) Štengl, V.; Králová, D. *Int. J. Photoenergy* **2011**, *2011*, 1–14.

(15) Bai, S.; Li, H.; Guan, Y.; Jiang, S. *Appl. Surf. Sci.* **2011**, *257*, 6406–6409.

(16) Shangguan, W. *Sci. Technol. Adv. Mater.* **2007**, *8*, 76–81.

(17) Gopidas, K. R.; Bohorquez, M.; Kamat, P. V. *J. Phys. Chem.* **1990**, *94*, 6435–6440.

(18) Yu, J.; Hai, Y.; Cheng, B. *J. Phys. Chem. C* **2011**, *115*, 4953–4958.

(19) Dinh, C.-T.; Nguyen, T.-D.; Kleitz, F.; Do, T.-O. *ACS Appl. Mater. Interfaces* **2011**, *3*, 2228–2234.

(20) Joo, J.; Kwon, S. G.; Yu, T.; Cho, M.; Lee, J.; Yoon, J.; Hyeon, T. *J. Phys. Chem. B* **2005**, *109*, 15297–15302.

(21) Li, X.-L.; Peng, Q.; Yi, J.-X.; Wang, X.; Li, Y. *Chemistry* **2006**, *12*, 2383–2391.

(22) Limaye, M. V; Singh, S. B.; Date, S. K.; Kothari, D.; Reddy, V. R.; Gupta, A.; Sathe, V.; Choudhary, R. J.; Kulkarni, S. K. *J. Phys. Chem. B* **2009**, *113*, 9070–9076.

(23) Sing, K. S. W.; Everett, D. H. W.; Haul, R. A.; Moscou, L.; Pierotti, J.; Rouquerol, J.; Siemieniewska, T. *Pure Appl. Chem.* **1985**, *57*, 603–619.

(24) Qian, S.; Wang, C.; Liu, W.; Zhu, Y.; Yao, W.; Lu, X. *J. Mater. Chem.* **2011**, *21*, 4945.

(25) Hu, H.; Kung, S.-C.; Yang, L.-M.; Nicho, M. E.; Penner, R. M. *Sol. Energy Mater. Sol. Cells* **2009**, *93*, 51–54.

(26) Hotový, I.; Huran, J.; Janík, J.; Kobzev, A. *Vacuum* **1998**, *51*, 157–160.

(27) Hotovy, I.; Huran, J.; Spiess, L.; Hascik, S.; Rehacek, V. *Sensors Actuators B Chem.* **1999**, *57*, 147–152.

(28) Zhu, H.; Yang, B.; Xu, J.; Fu, Z.; Wen, M.; Guo, T.; Fu, S.; Zuo, J.; Zhang, S. *Appl. Catal. B Environ.* **2009**, *90*, 463–469.

(29) Sabah, A.; Siddiqi, S. A.; Ali, S. *World Acad. Sci. Eng. Tech.* **2010**, *45*, 82–89.

(30) Dong, A.; Ye, X.; Chen, J.; Kang, Y.; Gordon, T.; Kikkawa, J. M.; Murray, C. B. *J. Am. Chem. Soc.* **2011**, *133*, 998–1006.

(31) Bao, N.; Shen, L.; Takata, T.; Domen, K. *Chem. Mater.* **2008**, *20*, 110–117.

(32) MA, G.; YAN, H.; SHI, J.; ZONG, X.; LEI, Z.; LI, C. *J. Catal.* **2008**, *260*, 134–140.

(33) Amirav, L.; Alivisatos, a. P. *J. Phys. Chem. Lett.* **2010**, *1*, 1051–1054.

(34) Ran, J.; Yu, J.; Jaroniec, M. *Green Chem.* **2011**, *13*, 2708.

(35) Sakai, N.; Ebina, Y.; Takada, K.; Sasaki, T. *J. Am. Chem. Soc.* **2004**, *126*, 5851–5858.

(36) Qi, L.; Yu, J.; Jaroniec, M. *Phys. Chem. Chem. Phys.* **2011**, *13*, 8915.

(37) Meissner, D.; Memming, R.; Shuben, L.; Yesodharan, S.; Grätzel, M. *Berichte der Bunsengesellschaft für Phys. Chemie* **1985**, *89*, 121–124.

(38) Davis, A. P.; Huang, C. P. *Water Res.* **1990**, *24*, 543–550.

(39) Weller, H.; Haase, M.; Spanhel, L.; Henglein, A. *Prog. Colloid Polym. Sci.* **1988**, *76*, 24–26.